

Photometric Selection of $z \sim 5$ Lyman Break Galaxies in the ESO Remote Galaxy Survey

L.S. Douglas^{1,2}, M.N. Bremer¹, E.R. Stanway¹ M.D. Lehnert² & D. Clowe³

¹H H Wills Physics Laboratory, Tyndall Avenue, Bristol, BS8 1TL, UK

²Laboratoire d'Etudes des Galaxies, Etoiles, Physique et Instrumentation GEPI, Observatoire de Paris, Meudon, 92195, France

³Department of Physics and Astronomy, Ohio University, 251B Clippinger Lab, Athens, OH 45701, USA

Accepted . Received ; in original form

ABSTRACT

We describe the selection of a sample of photometrically-defined Lyman break galaxies (LBGs) at $z \sim 5$ using the multi-wavelength imaging data of the ESO Remote Galaxy Survey (ERGS). The data is drawn from ten widely-separated fields covering a total sky area of 275 arcmin². Starting with a simple colour ($R - I > 1.3$) and magnitude ($I < 26.3$) cut to isolate the Lyman break and then refining the sample by applying further optical and near-infrared photometric criteria we identify a sample of 253 LBG candidates. We carefully model the completeness of this sample and the factors that affect its reliability. There is considerable overlap between this sample and a spectroscopically-confirmed sample drawn from the same survey and this allows us to determine the reliability of the optical photometric selection (~ 60 per cent) and to show that the reliability can be significantly improved (to ~ 80 per cent) by applying near-infrared waveband criteria to exclude very red contaminants. Even this high level of reliability may compromise some statistical studies of LBG properties. We show that over 30 per cent of the highest reliability candidates have multiple UV-luminous components and/or disturbed morphology in HST imaging, though it is unclear whether this represents multiple interacting/merging sources or individual large sources with multiple UV bright regions. Using this sample we confirm that the normalisation of the bright end of the $z = 5$ UV luminosity function (down to M^*) is lower than the same at $z = 4$ by a factor of 3. Using a Schechter fit we determine $M_{UV}^* = -20.9 \pm 0.2$. We discuss whether it is reasonable to expect the UV luminosity function to follow a Schechter function, given the UV emission is short-lived and stochastic, and does not necessarily trace the underlying mass of the galaxy.

Key words: Galaxies; high redshift, luminosity function, starburst.

1 INTRODUCTION

Until the turn of the century, very few spectroscopically-confirmed galaxies at $z \sim 5$ and above had been identified and fewer still studied in any detail. Given that this redshift range covers the first billion years after the Big Bang, this meant that there was little concrete evidence of how early galaxy formation proceeds. With the advent of deep imaging with 8m ground-based telescopes, and with the GOODS and HUDF projects carried out with HST, it has become possible to photometrically identify distant galaxy candidates and potentially confirm them through spectroscopy.

By extending the Lyman break technique (Guhathakurta et al. 1990; Steidel & Hamilton 1992, 1993), to $z \sim 5$ using R, I and z -band imaging, Lehnert & Bremer (2003) showed that with the right observational setup it

is now possible to securely identify multiple high redshift galaxies in individual 8m telescope pointings. These Lyman Break Galaxies (LBGs) are identified *via* their redshifted UV continuum emission arising from strong unobscured star formation within the systems. Subsequently, similar studies have been carried out by other authors in order to select galaxies with redshifts above $z = 4.5$ (Ouchi et al. 2004) and potentially to $z > 6$ (e.g. Stanway et al. 2003, 2004, 2008a).

While some of these studies have included spectroscopic confirmation of samples derived from photometry, many others have not. These have relied on the high success rate of spectroscopic confirmation in previous work (e.g. Lehnert & Bremer 2003, confirmed six of a sample of twelve candidates in a 40 arcmin² field to be at $4.8 < z < 5.8$) to argue that photometric selection was reliable enough to carry

out statistical studies on photometric samples. However, as shown by Stanway et al. (2008b), the reliability and completeness of such samples depends on a complex combination of factors, particularly the filter set and CCD response used to carry out the imaging. In the absence of spectroscopy, other data is required to help exclude contaminating galactic stars and $z \sim 1$ elliptical galaxies from photometric samples, such as HST and/or deep near-IR ground-based imaging. One of the main advantages of purely photometric samples is that they can cover a relatively large area of sky in comparison to spectroscopic samples. However, given the difficulty of obtaining HST and near-IR data of sufficient depth over a large sky area, the use of photometric samples are often compromised.

For this reason, despite the apparent ease of defining a photometric sample, there are distinct advantages in using a sample which has clear spectroscopic evidence of reliability when attempting to understand the statistics and other properties of star forming galaxies at $z > 5$. Accurate determinations of their clustering statistics, luminosity functions, star formation histories, stellar population properties and contribution to reionization all require an understanding of the contaminants in the sample being used for the study. Adding to this the need for accurate redshifts in order to carry out many detailed studies of individual high redshift systems, the need for a well-defined photometric sample of $z \sim 5$ LBGs with good spectroscopic follow-up is clear.

Lehnert & Bremer (2003) showed that it was possible to obtain ground-based samples of such objects with a reasonable level of spectroscopic confirmation. However, the study covered a comparatively small area of sky and so could only be used to determine the simplest of statistical properties for such sources. In more recent years larger areas have been covered by spectroscopic programs e.g. Ando et al. (2007) and Vanzella et al. (2009) which confirmed 10 and 32 high redshift galaxies respectively. Although these surveys are important to the understanding of the selection of high redshift galaxies and their properties, they often only target the brightest candidates spectroscopically or do not uniformly probe the corresponding photometric sample. One of the goals of this survey, described here and in future papers, is to observe many high redshift LBG candidates over a range of luminosities and colours to discover if the relatively high completeness seen in previous studies is applicable at fainter magnitudes. Although the level of contamination of low redshift Lyman break galaxy samples are often very low, *e.g.* Steidel et al. (2003), such a low level cannot be assumed for higher redshift samples. The differences in the selection functions and colours used mean that the two samples are contaminated by completely different galactic and extragalactic populations.

To address this, and other, goals we have carried out a large programme of imaging and spectroscopic observations which cover a sky area fourteen times larger than the original Lehnert & Bremer (2003) study including an expanded region of ~ 160 arcmin 2 centered on the original Lehnert & Bremer (2003) pointing. This paper introduces the imaging data sets used to generate a sample of $z \sim 5$ LBG candidates which were followed-up by the same spectroscopic setup used in the original Lehnert & Bremer (2003) work. Also it describes a photometric sample of $z \sim 5$ LBG candidates with well-determined reliability and com-

pleteness which can be used for statistical study, such as a determination and discussion of the $z \sim 5$ LBG UV luminosity function presented here and a brief comparison of the results of a single $R - I$ colour cut to that of a sample selection with an additional $I - z$ criterion.

The data presented here are drawn from ten ~ 40 arcmin 2 fields widely-separated on the sky. Observations were carried out as part of an ESO Large Programme, “The ESO Remote Galaxy Survey”, or ERGS (PI M. Bremer, ID 175.A-0706). This capitalised on existing deep optical imaging of multiple fields already obtained by the ESO Distant Cluster Survey (EDisCS) project (White et al. 2005), itself an ESO Large Programme (PI S. White, ID: 166.A-0162). The resulting spectroscopic sample of ERGS contains many tens of high redshift galaxies with secure redshifts (Douglas et al. 2009).

The structure of this paper is as follows. In section 2 we discuss the imaging data that was used as a basis for this work and briefly describe follow-up spectroscopic observations. In section 4 and 4 we discuss the photometry and how the candidates were selected. We then discuss the final sample in section 5 and the estimated contamination fraction. The completeness of this sample is described in section 6. The morphology and observed UV luminosity function for the high redshift LBG candidates is considered in sections 7 and 8

We adopt the standard Λ CDM cosmology, i.e. a flat universe with $\Omega_\Lambda = 0.7$, $\Omega_M = 0.3$ and $H_0 = 70 \text{ km s}^{-1} \text{ Mpc}^{-1}$. All photometry was determined in the AB magnitude system (Oke & Gunn 1983).

2 OBSERVATIONS AND DATA

In order to select a sample of objects containing $z \sim 5$ LBGs all that is needed in principle is sufficiently-deep R and I -band imaging. Selecting a flux limited sample in I containing objects with an $R - I$ colour redder than a particular value (usually $R - I > 1.3$ or $R - I > 1.5$) should identify a sample of $z \sim 5$ LBGs with a completeness that depends on the statistical quality of the data. However, to *cleanly* select a sample of high redshift galaxy candidates without being swamped by contaminating cool Galactic stars and lower redshift galaxies, a wide range of multi-band deep imaging is required.

2.1 Imaging

The data set used in this study includes optical imaging using the V , R , I and z bands, near infrared imaging in the J and K_s bands and complementary high resolution I -band imaging from the Hubble Space Telescope (HST) of ten widely separated fields each of size ~ 40 arcmin 2 . The high Galactic latitudes of these fields result in minimal Galactic extinction effects and the original selection of the fields to observe $z \sim 0.7$ clusters produced an effectively random sampling of the sky at $z \sim 5$, reducing the effects of cosmic variance.

The majority of the imaging data were taken as part of EDisCS (White et al. 2005), a photometric and spectroscopic survey of galaxy clusters selected from the Las Campanas Distant Clusters Survey (Gonzalez et al. 2001). The

observing programme involved deep optical imaging using FORS2 at the VLT, near-infrared imaging using SOFI at the NTT, and high resolution imaging using the ACS camera on HST. The fields were observed with FORS2 in the V , R , and I bands for approximately 2 hours each, with a field of view after dithering of $6.5' \times 6.5'$. In the near-infrared, the fields were observed using SOFI on the NTT in the J - and K_s -bands for at least 300 and 360 minutes respectively. The effective field of view of the near IR observations was typically $5.4' \times 4.2'$, consequently only around 50 per cent of each optical field was covered. This ground based imaging was complemented by 80 orbits of HST/ACS imaging (Desai et al. 2007). Nine of the ten fields were observed for one orbit over the whole field and an additional four orbits in the central region using the F814W filter, with over 80 per cent of each ground-based optical field being covered by HST data. With typical seeing conditions for the ground based observations between $0.5''$ and $0.8''$, the 2σ depth in a $2''$ diameter aperture of each image was typically 28.1 in the V -band, 27.9 in the R -band, 27.1 in the I -band, 24.5 in the J -band and 23.7 in the K_s -band. Details can be found in Table 1. The depths of the images were calculated by measuring the noise properties of multiple randomly placed $2''$ apertures in background areas of the images.

These images were reduced using standard techniques for bias and bad pixel removal and flat fielding. The software IMCAT *findpeaks* was used to detect local minima in images smoothed with a $1''$ Gaussian to create a catalogue of local sky measurements. These measurements were then fitted to a bi-cubic polynomial and subtracted from the unsmoothed image. The images were also aligned with known stars in the USNO catalogue to correct for camera distortions and the linear offset between the fields, preserving the surface brightness. Specific details of the data reduction producing the calibrated images used in this study can be found in White et al. (2005).

2.1.1 Additional z -band Imaging

The high redshift galaxies selected in this project are observed due to their bright rest-frame UV emission, redshifted to ~ 740 nm at $z \sim 5$, arising from vigorous star formation within the galaxies. As young star forming galaxies, they are expected to have approximately flat continuum emission ($f_\nu = \text{constant}$, an AB colour of zero) longward of Lyman α which can be probed in the observed z -band. In the absence of other effects, the $I-z$ colour can also be an indication of a galaxy's redshift as the Lyman break moves through the I -band, ($5.0 < z < 5.8$). A high $I-z$ colour would indicate very little flux in the I -band caused by the Lyman break located near the red edge of the I -band filter. Thus, the addition of z -band imaging can improve photometric selection of high redshift galaxy candidates and the ability to study a candidate's properties.

Each of the ten separate fields were observed for two hours in the z -band with FORS2 (Appenzeller et al. 1998) using the z -Gunn filter and 2×2 pixel binning. The observations were carried out in March and December of 2005 and February and March of 2007. For each field, forty-two exposures of two minutes each were taken at slightly different dither positions, similar to the technique used in the near infrared. Many short exposures are needed to minimise the

increasing night sky emission at redder wavelengths. The high background is caused by line emission from the excited levels of the hydroxyl radical OH^- . This airglow can vary on timescales as short as five minutes so having many short exposures is beneficial. The fields have a mean depth of 26.18 AB magnitudes (2σ limit in a $2''$ aperture) for an 84 minute observation. The observations were taken with the same instrument as the other optical imaging and the exposures were planned to match the field of view of the existing images. The reduction of the data followed standard techniques using *IRAF* software. Bias subtraction, flat-fielding, bad-pixel removal and photometric calibration using standard star observations were all performed in the standard manner.

Although the data were obtained with the same camera as that used to obtain the V , R and I -band datasets, in the time between the two sets of observations, the CCD chips were upgraded from SiTE SI-424A backside thinned devices to MIT/LL devices. This upgrade improved the quantum efficiency of the instrument in the z -band, and almost completely removed any fringing longward of 8000\AA . It also changed the pixel scale of the data (from 0.2 to 0.125 arcsec per unbinned pixel), a change that influences how we carry out the photometry discussed section 3.

2.2 Spectroscopy

In addition to the z -band imaging, the ERGS program spectroscopically observed a range of high redshift candidates and intermediate and low redshift contaminating objects. Although the spectroscopic follow-up will be presented in detail in a forthcoming paper, a brief summary is given as some of the results will be referred to in sections 4 and 5.

The high redshift galaxy candidates were followed-up spectroscopically in a 100 hours VLT/FORS2 program described in Douglas et al. (2009). The 10 survey fields were observed using 20 spectroscopic masks on VLT/FORS2 each containing 30 to 40 slitlets with a width of 1 arcsec and typical length of 10 arcsec. Observations were carried out in service mode between December 2005 and May 2007 during dark time with seeing conditions better than 1 arcsec and clear or photometric conditions at an airmass less than two. Each mask was observed for 3.6 hours divided into exposures of 650 seconds nodded along the slit to avoid the effect of pattern noise or bad pixels and facilitate the best possible sky subtraction. FORS2 was used in spectroscopic mode using the R300I grating with the OG525 blocking filter to restrict the wavelength range to between 650-1000nm. The resulting pixel scale was 3.2\AA in the spectral direction and 0.2 arcsec spatially and the spectral resolution was $\sim 13\text{\AA}$, measured from the width of the sky lines.

The data were reduced following the same standard procedures as those described in Lehnert & Bremer (2003) and hence consistent with the data in the previous work. More details of the spectroscopic data reduction and analysis will be presented in Douglas et al. (2009).

3 PHOTOMETRY

Object catalogues were initially created from the fully reduced and calibrated images using the galaxy photometry

Table 1. Magnitude limits for 2σ detections in a $2''$ circular aperture. The mean weak lensing corrections for each field, as calculated from the maps of Clowe et al. (2006), are shown in the last column.

Field	V	seeing	R	seeing	I	seeing	z	seeing	J	seeing	K _s	seeing	Lensing mag
J1037.9-1243	28.11	0.55''	28.04	0.54''	27.00	0.56''	26.17	0.57''	24.61	0.82''	23.93	0.82''	0.12
J1040.7-1155	28.08	0.65''	27.95	0.72''	26.94	0.62''	26.12	0.77''	24.56	0.70''	23.49	0.68''	0.08
J1054.4-1146	28.04	0.67''	28.07	0.78''	27.04	0.72''	26.03	0.58''	24.32	0.83''	23.53	0.68''	0.24
J1054.7-1245	28.07	0.79''	27.94	0.77''	27.24	0.50''	26.10	0.62''	24.45	0.82''	23.72	0.78''	0.26
J1103.7-1245	28.05	0.83''	28.01	0.75''	27.19	0.64''	26.23	0.55''	24.38	0.77''	23.56	0.63''	0.20
J1122.9-1136	28.12	0.71''	28.00	0.70''	27.19	0.65''	26.20	0.55''	24.51	0.79''	23.59	0.61''	0.11
J1138.2-1133	28.07	0.58''	27.86	0.68''	27.14	0.60''	26.14	0.65''	24.59	0.82''	23.69	0.82''	0.17
J1216.8-1201	28.05	0.68''	27.92	0.72''	27.16	0.60''	26.23	0.50''	24.50	0.76''	23.58	0.67''	0.37
J1227.9-1138	28.09	0.73''	27.89	0.83''	27.12	0.74''	26.27	0.65''	24.62	0.96''	23.67	0.70''	0.08
J1354.2-1230	27.92	0.70''	27.96	0.70''	27.16	0.66''	26.35	0.45''	24.51	0.90''	23.98	0.74''	0.13

package SExtractor version 2.4.4 (Bertin & Arnouts 1996). Magnitudes were determined using both $2''$ circular apertures and SExtractor defined MAG_AUTO apertures, which gave the best estimate of total magnitudes for individual objects. Aperture corrections were determined for the circular apertures from the photometry of relatively isolated stars (identified as such using the HST imaging) using larger apertures. A comparison of the corrected circular aperture and MAG_AUTO aperture photometry for a range of unresolved sources showed agreement within statistical uncertainty.

All high redshift candidates were expected to be unresolved in the ground-based imaging (they are found to have half-light radii of around $0.1''$ - $0.3''$, Bremer et al. 2004, compared to typical seeing of $0.7''$). The original intention was to apply the MAG_AUTO apertures to the other imaging bands with small corrections (usually a few hundredths of a magnitude) for differences in seeing in order to determine colours, or limits on colours. This required resampling the z , J and K_s -band images to the same pixel-scale and astrometry as that of the V , R and I -bands. Unfortunately the resampling significantly correlated the noise in the background, particularly in the z -band. This had a significant effect on the photometry of the faint ($z > 25$) LBG candidates (see figure 1). Consequently, all subsequent photometry was carried out using $2''$ circular apertures on images which have not been resampled, taking into account the appropriate aperture corrections. This resampling did not affect the V , R and I images so we were able to additionally select objects which had colours that fell into our selection criteria in the MAG_AUTO photometry for these bands. While not part of our main photometric sample discussed here, these were included on spectroscopic slit masks where there was available space.

SExtractor was used in two image mode, assigning the I -band image as the detection image with which to define the photometric apertures for the three bluest images, V , R and I -band as these images were taken with the same pixel scale and central pointing. Objects were identified by a flux excess of more than 1.5σ over at least four consecutive pixels. For the redder bands the I -band image was used as a detection image to define the centers of the apertures. These RA and

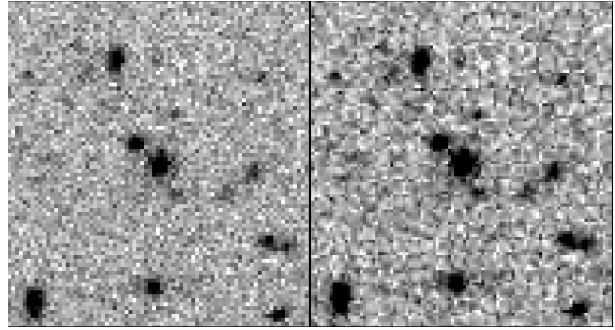


Figure 1. The image on the left shows a portion of the fully reduced z -band image where no rebinning has taken place. The image on the right is of the same portion of the reduced z -band image rebinned to match the I -band image. The correlated pixel noise can be seen as a rectilinear pattern covering the background.

Dec positions were used to place appropriately scaled $2''$ apertures on the z , J and K_s -band images.

SExtractor does not carry out photometry of an arbitrary list of celestial coordinates. Consequently, this latter photometry was carried out using a modified version of the APER routine in the IDL astronomical library. In each case the photometry was carried out on images which had been background subtracted by SExtractor, using the APER routine without any background subtraction, in order to mimic as closely as possible the photometry carried out in the bluer bands. The code was checked by comparing the resulting photometry of the I -band frame with that from SExtractor, both giving consistent results.

The resulting catalogue containing V -, R -, I -, z -band photometry for all objects detected in the I -band, along with J and K_s photometry for those objects covered by the near-IR imaging, was then corrected for Galactic extinction (Schlegel et al. 1998) producing the final photometry catalogue used for high redshift candidate selection. The uncertainties in the measurements were assessed by placing artificial galaxies of known size and flux randomly on the science image and then recovering them using the above methods. It was found that the measured errors approached

the theoretical Poissonian statistical error. Had an optimised aperture been used, such as the MAG_AUTO isophotal apertures used by SExtractor, the measured errors would have reproduced the statistical errors. In cases where objects were undetected in a single band, the 2σ magnitude limit in a $2''$ diameter aperture was used to determine colours.

These fields were originally chosen to study $z \sim 0.8$ galaxy groups and clusters as part of the EDisCS project (White et al. 2005). Each field contains a clustered system at $0.6 < z < 0.8$ with velocity dispersions generally between $300 < \sigma < 900 \text{ km s}^{-1}$. One has a velocity dispersion of $\sim 1000 \text{ km s}^{-1}$. These systems have a weak lensing effect across the fields and potentially a strong lensing effect over a small area. We used the lensing models derived by Clowe et al. (2006) to determine the position-dependent amplification for sources at $z \sim 5$ in order to determine the magnitudes of the sources in our (observed) flux limited catalogue in the absence of the intervening systems. These corrections were typically of ~ 0.1 magnitudes and we found no strongly-lensed $z \sim 5$ candidates. The lensing effect was achromatic, changing the total magnitudes of objects but not their colours.

4 LGB CANDIDATE SELECTION

To take advantage of the near-IR imaging within this data set we use the following selection method, described step-by-step, to produce a robust sample of LBG candidates. The optical V -, R - and I -bands are used to select a flux limited sample with a continuum break which, if identified as the Lyman break, places the sources at $z > 4.8$ (described in sub-section 4.1). The near-IR imaging then becomes critical in identifying common low redshift stars and galaxies with colours red enough to satisfy the optical criteria. Having described such interlopers in sub-section 4.2, sub-section 4.3 discusses the impact of the additional near-IR criteria. This leads to the final high redshift LBG candidate sample in section 5 which includes a discussion on the contamination fraction estimate from spectroscopic observations of a subset of the sample.

4.1 Optical Selection Criteria

In order to identify objects with the characteristic spectral break between the I - and R -band of high redshift star forming galaxies, the selection criteria of $I < 26.3$ and $R-I > 1.3$ were imposed to create a catalogue of objects with a significantly large spectral break or a non-detection in the R -band. An additional condition of $V > 27.5$ was added as this band samples light around the Lyman limit at $z \sim 5$. As such, very little, if any, flux is expected at these wavelengths. Although applying this V -band cut will exclude a few per cent of the high redshift galaxies (typically those at redshifts $4.7 < z < 5.0$ and magnitudes $I < 25.5$), it has the effect of decreasing the sample size by about 40 per cent and so substantially decreases the contamination fraction (see simulations in section 6).

Including only those areas which are covered by all imaging bands (V -band to K -band) and excluding regions near bright sources, a total of 319 objects were identified over the 10 survey fields covering an area of 275 arcmin^2 .

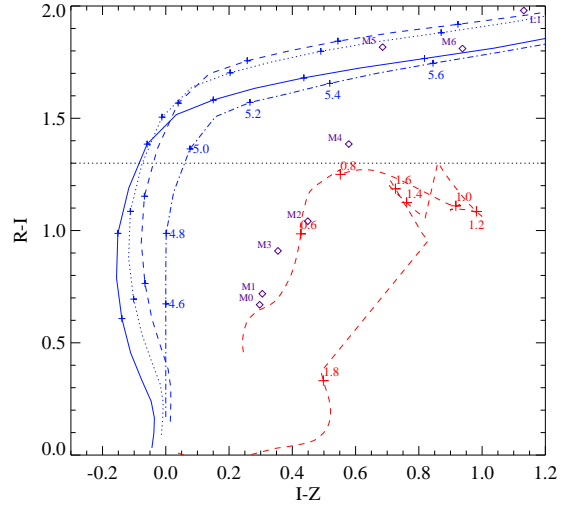


Figure 2. Colour modelling of high redshift star forming galaxies (blue) using a variety of stellar ages. A simple SED flat in f_ν is represented by the dash-dot line. The other three colour tracks are star forming galaxies from Maraston (2005) with increasing stellar age of 10 Myrs (solid line), 100 Myrs (dotted line) and 400 Myrs (dashed line). All have had appropriate IGM absorption applied as described in the text. Also shown are intermediate redshift elliptical galaxies (red) from Maraston (2005) models, assuming a formation redshift of $z=5$ and a star formation e-folding time of $\tau=0.5 \text{ Gyr}$, and cool, low mass stars with labels indicating subtype (purple) from Hawley et al. (2002) templates, using appropriate FORS2 filter set for this study. Redshifts are noted for the high and intermediate redshift galaxies.

Figure 2 shows the expected optical colour evolution of a high redshift LBG represented by the blue solid, dotted and dashed lines labelled from redshifts of 4.6 to 5.6. The dot-dash line represents a SED which is flat in f_ν and the solid, dashed and dotted blue lines are star forming galaxies taken from Maraston (2005) integrated galaxy spectral synthesis models (updated PEGASE models (Fioc & Rocca-Volmerange 1997) of the same age produce similar colours). Each track represents a different stellar age, 10 Myrs (solid), 100 Myrs (dotted) and 400 Myrs (dashed), the oldest reasonable stellar age given the redshift range probed.

All models have been adjusted for the effects of absorption by intervening hydrogen clouds in the intergalactic medium (IGM). We use the models of Madau et al. (1999) for the evolution in the number density and column density distribution of hydrogen clouds in the IGM to estimate the absorption as a function of redshift due to the Lyman-series and Lyman limit. In common with other authors (e.g. Bouwens et al. 2007), we modify the original Madau models to account for the higher absorption seen in the spectra of high redshift quasars (Songaila 2004) by requiring a more rapid evolution in the number density of absorbing clouds (*i.e.* $(1+z)^3$ rather than $(1+z)^{2.46}$) beyond $z=4.5$.

As the stellar age increases, the colours of the galaxies become redder. Although models with varying extinctions are not shown here to maintain the clarity of figure 2, there is a similar reddening effect with increasing extinctions. Ap-

plying the Calzetti et al. (2000) dust model to the galaxy models shown, the $R - I$ colour reddens by ~ 0.2 magnitudes and the $I - z$ colour by ~ 0.1 magnitudes per 0.1 increment in E(B-V) from 0 to 0.5. Given the single $R - I$ colour cut used in this work we are able to include any I -band selected candidate regardless of its intrinsic continuum slope and corresponding $I - z$ colour. Results from the spectroscopic follow-up suggest that the majority of $z \sim 5$ LBGs have intrinsically blue colours in the observed optical bands at wavelengths shorter than the Balmer break with little reddening, despite the fact that much redder objects could have been observed, justifying the use of relatively blue galaxy models in understanding the optical selection function. While older, redder objects do exist at $z \sim 5$ (e.g. Verma et al. 2007), they are a minority population.

The single colour selection used here could have introduced a high number of candidates which are only detected in a single band potentially leading to a larger number of spurious sources caused by noise spikes. Our spectroscopy shows that this is not the case. Within the photometric selection there were 40 objects with a single band detection in the I -band. Of these, 15 were observed spectroscopically down to the faintest I -band magnitudes and only one was not detected in the continua of the subsequent spectra. In the complete spectroscopic program (Douglas et al. 2009), which targeted fainter and bluer objects, an additional 10 objects were only detected in the I -band to $I < 26.3$ and all of which had continuum spectroscopically detected and are therefore real objects.

These spectroscopic results suggest only one of 25 observed sources could be spurious giving an upper limit of 4% of the single band detections for the fraction of spurious sources. At these faint magnitudes, a lack of spectral flux is not conclusive evidence that such a source is spurious. Thus, this upper limit could be a considerable overestimate. Assuming the spectroscopic results are representative there are, at most, only 2 objects within the sample predicted to be spurious and as such, this is not treated as a significant problem.

The number of spurious sources was also checked by performing identical source detection routines on inverted images. No spurious sources were identified using this method.

4.2 Common Red Interlopers

While a simple two or three-band colour cut can efficiently select a sample of distant LBGs, such a sample will inevitably include low mass Galactic stars and intermediate redshift passively evolving or reddened galaxies (Stanway et al. 2008b) even without photometric scatter. By using the additional near-IR photometry we can substantially decrease the number of these interlopers in our final sample.

The first major potential interlopers that we need to consider are cool, low mass Galactic stars. To estimate accurate colours for the stellar interlopers applicable to the specific filter set used here, the stellar templates derived by Hawley et al. (2002) were processed through the FORS2 filter set including detector response. Figure 2 shows the $R - I$ and $I - z$ colours for M-type dwarfs. It shows that late M-types will be included in the sample with a $R - I > 1.35$. Figure 3 shows Knapp et al. (2004) near-IR stellar spectra

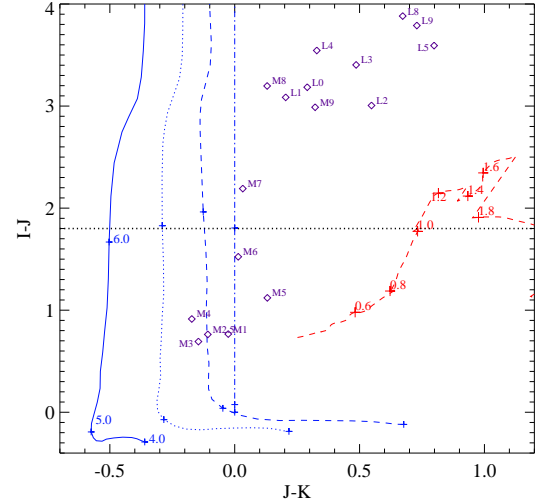


Figure 3. Colour modelling high redshift star forming galaxies, intermediate redshift ellipticals and low mass stars as described in figure 2. The dotted line represents the 2σ colour limit of the $I - J$ colour at the flux limit of the sample.

convolved with the appropriate filter set. It shows that the $J - K_s$ colour is relatively flat for M- and L-type dwarfs, however a larger range is observed in the $I - J$ colour spanning from 0.8 for the early M-type dwarfs to 3.5 for the late L-type dwarfs.

The $2-\sigma$ magnitude limits for our near-IR data are typically $J < 24.5$ and $K_s < 23.7$. Given these near infrared depths late M-type and L-type dwarfs should be excluded from the high redshift sample through their $I - J$ and $J - K_s$ colours with limits of $I - J > 1.8$ (shown by the black dotted line in figure 3) and $J - K > 0.8$ for near-IR detections. Although early-type M-stars are not red enough to be detected in the near infrared imaging at the flux limit of the sample, their relatively blue optical colours ($R - I \leq 1$) would exclude them from the high redshift selection. By contrast, true LBGs are expected to have relatively flat colours with $I - J < 1.8$ and $J - K < 0$ (Verma et al. 2007) and as such should not be detected in the near-IR imaging. As we note later, an advantage of using a single $R - I$ colour cut is that it includes intrinsically red objects. However, as noted previously, the majority of spectroscopically confirmed high redshift galaxies had relatively blue continuum, supporting the use of the comparatively blue models.

By incorporating the redder near-IR wavebands into the selection criteria we can exclude late M-type and L-type dwarf stars and early M-types from M1 to M3. The only stellar populations which have colours that can not be isolated using this imaging data set are M4 to M6 dwarf stars. However, the number density of M-stars is expected to decrease with fainter magnitudes.

The other major potential interloper of high redshift samples are the class of intermediate redshift elliptical galaxies often referred to as EROs (extremely red objects). Such interlopers have a redshift between 0.5 and 2.0 and have redder optical to near-IR colours than the high redshift star bursting galaxies. Figure 2 shows the RIZ colour evolution for a passively evolving intermediate redshift source. This

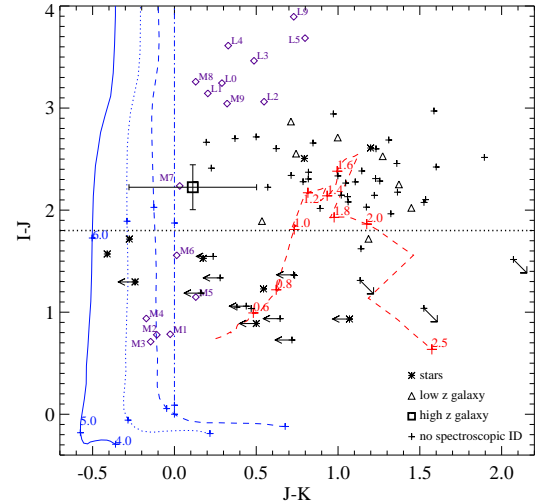
population of galaxies could enter the selection around a redshift of $z = 0.8 - 1.6$, where the 4000Å break falls in the I -band. When combined with the underlying red colour of a passively evolving stellar population, this can lead to intermediate redshift objects with sufficiently red $R - I$ colours falling into the simple colour selection. However, these objects can again be identified and removed from the high redshift sample using near-IR imaging of sufficient depth. Different levels of dust could also redden these intermediate redshift galaxies in the optical encroaching them into the high redshift selection. Due to the I -band selection, dust reddening would lead to bright z , J and K_s colours leading to such galaxies being rejected from the sample by the near-IR criteria in sub-section 4.3.

The intermediate redshift galaxy model from figure 2 is plotted in figure 3 which illustrates the $I - J$ and $J - K_s$ colour evolution. The model indicates that at a redshift of $z \gtrsim 1.0$ the galaxies would be detected in the near-infrared imaging with an $I - J$ colour redder than the limits of the imaging even at the flux limit of $I = 26.3$. Intermediate galaxies at lower redshifts ($z < 1$) are in principle removed by the initial optical selection, however stochastic photometric uncertainties may cause them to reenter the sample.

Although the near-infrared data available to this study is not deep enough to detect the individual high redshift candidates, the colours calculated above imply that many lower redshift interlopers (early and late M-type and L-type dwarf stars and ellipticals at $z > 1$) are detectable and can be identified. As such, any candidate with a clear near-infrared detection was removed from the high redshift galaxy sample. As figure 3 shows, galaxies at $z \sim 5$ are not expected to be detected in the near-IR imaging. Only galaxies with a high extinction, reddening the optical to near-IR colours, could expect to be detected. For the mean I -band magnitude of the sample, two magnitudes of reddening in the K_s -band would be required for the object to be detected in the K_s -band imaging. Studies such as those of Verma et al. (2007), which model the spectral energy distribution of similar high redshift galaxies, expect relatively low extinctions making such dusty objects rare. From Monte Carlo simulations using the probability distributions of models rather than the formal best fitting scenario, Verma et al. (2007) found no objects with reddening greater than one magnitude and less than 10% of the formal best fitting models had sufficient reddening to be detected in the ERGS K_s -band imaging. Hence, removing all objects with a near-IR detection will reduce the interloper fraction while not significantly effecting the completeness of the high redshift sources given the rarity of sufficiently dusty sources.

4.3 Near-IR selection criteria

Using the near-IR imaging to identify common interlopers we exclude objects with $J < 24.5$ and/or $K_s < 23.7$ from the LBG sample. At close to the I -band limit these near-IR limits indicate colours incompatible with a high redshift identification (figure 4). The effect of the near-IR colour cut is to exclude 66 objects. Within this sample 63 objects had $I - J > 0.7$ and $J - K > 0.1$ separating them from the theoretical colours of low extinction high redshift galaxies. The three remaining objects had blue $J - K$ colours approaching the high redshift colour tracks. However, all these



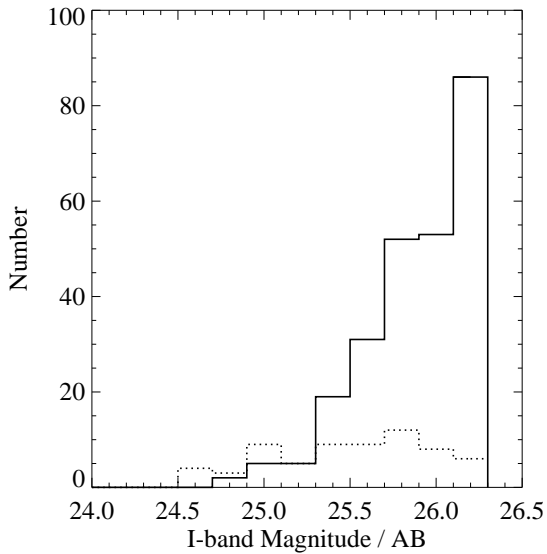


Figure 5. Distribution of observed I -band magnitudes of final photometric sample (solid line) with near-IR detected sources rejected and the sources removed from the sample because of near-IR detections (dotted line).

function rather than the comparatively steeper exponential bright-end, assuming a typical Schechter function fit to the $z = 1$ luminosity function. With the candidate high redshift galaxy number counts increasing towards fainter magnitudes this results in a lower fraction of intermediate redshift galaxies at $I > 26$.

5 THE $Z \sim 5$ GALAXY CANDIDATE SAMPLE

The final photometric selection consisted of 253 objects in the refined sample, all with multiband photometry consistent with a redshift of $z \sim 5$ or higher, using the strict criteria discussed above. Figure 5 shows the observed I -band flux distribution for the refined sample of 253 objects and the 66 removed because of their near-IR detections.

Significant field-to-field variation in the number of high redshift candidates was observed as shown in table 2. The range of number densities observed for the refined sample in individual fields can not be explained by cosmic variance when using the estimator of Trenti & Stiavelli (2008) suggesting observations of truly under and overdense fields. In contrast, the variation in the number density of near-IR detected sources can be explained by cosmic variance, estimated by Trenti & Stiavelli (2008) assuming a lower redshift ($z=1$), with the exception of only two fields.

5.1 Single versus two colour cut

Due to the shapes of the filter bandpasses and the typical colours of low mass stars, a two colour selection, *i.e.* criteria in $R - I$ and $I - z$ colours, is unable to efficiently select high redshift galaxies while eliminating M-type dwarf stars. Given this and the range of $I - z$ colours predicted for high redshift objects, a single $R - I$ criteria was adopted. While

Table 2. Source density per arcmin² for each survey field.

Field	Refined sample	Near-IR sources
J1037.9-1243	0.47	0.23
J1040.7-1155	0.85	0.26
J1054.4-1146	0.26	0.22
J1054.7-1245	2.09	0.19
J1103.7-1245	0.67	0.18
J1122.9-1136	0.65	0.52
J1138.2-1133	0.64	0.07
J1216.8-1201	1.55	0.26
J1227.9-1138	0.78	0.21
J1354.2-1230	1.29	0.25

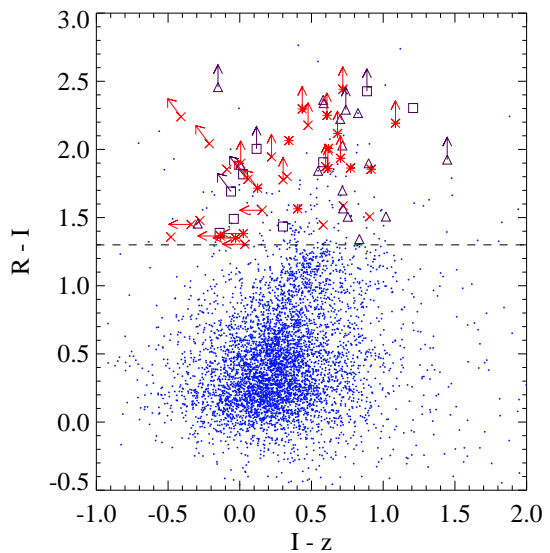


Figure 6. Colour-colour diagram showing spectroscopically confirmed high redshift galaxies (crosses - line emitters, asterisks - continuum breaks) and confirmed lower redshift objects (galaxies and stars where squares are objects undetected in nIR imaging and triangles are objects detected in nIR) compared to the field populations (points). Arrows represent 2σ colour limits when there is no detection in corresponding band.

the absence of an $I - z$ colour cut may lead to a higher contamination fraction in a purely optically selected sample, the addition of near-IR selection criteria minimise this effect as discussed in section 4.

The $R - I$ and $I - z$ colours of the spectroscopically observed sources within the photometric sample are shown in figure 6. The small dots show the range of colours seen in the catalogue of all objects in a single field. Over-plotted are the objects which were spectroscopically confirmed to be at high redshift (asterisks are galaxies identified using only their continuum break and crosses are galaxies identified with Ly α line emission) and confirmed lower redshift galaxies and stars with and without near-IR detections (triangles and squares respectively). A number of sources, spectroscopically confirmed to be low redshift galaxies or galactic stars, have $I - z$ colours bluer than that expected from the mod-

els in figure 2. This is most likely caused by a combination of photometric errors and different intrinsic properties of the sources to that assumed in the models. Figure 6 illustrates that without the near-IR imaging many low redshift objects would not be distinguishable using only the optical colours. Also, had an $I - z$ colour criteria been applied to eliminate lower redshift contaminants, many high redshift galaxies would have been excluded from the sample.

A variety of $R - I$ and $I - z$ colour cuts could be used to isolate the stellar interlopers from the LBG candidate sample, *e.g.* $I - z < 0.5$. Adopting this additional colour cut should, in principle, exclude any stellar interlopers, however for the case of $I - z < 0.5$, 36% of the spectroscopically confirmed high redshift sources would be rejected from the sample and only three of the nine spectroscopically confirmed lower redshift interlopers would be removed. Thus, the application of such a colour cut for this combination of filters would significantly reduce the number of high redshift candidates biasing the sample to blue rest-frame UV continuum, while not significantly reducing the relative contamination.

The additional near-IR selection criteria is an effective substitute for an $I - z$ colour cut, removing common interlopers without influencing the high redshift LBG sample.

5.2 Contamination Fraction from Spectroscopic Observations

It is possible that for the optically-fainter objects we fail to reject contaminants because they are too faint to be detected in the near-IR data. At the flux limit of the sample there is a colour limit of $I - J < 1.8$ and $I - K_s < 2.6$ which does not exclude all possible low redshift contaminants even in the absence of photometric scatter. Lower redshift objects can also scatter into photometric selections through photometric error and extreme colours.

Our spectroscopic programme was optimised to maximise the number of spectroscopically-confirmed $z \sim 5$ objects and had sufficient slits to sample robustly all objects which obeyed the optical selection. Consequently we were able to test if a given selection criteria improved the sample. A third of all photometric candidates with a range of I -band flux, colours and near-IR detections were observed. The spectroscopic identifications of this subsample can be used to estimate the fraction of contamination in the refined photometric high redshift sample. Although a spectroscopic identification is harder to achieve for intrinsically fainter objects, figure 7 shows that our confirmed high redshift LBGs are not biased to brighter I -band magnitudes and have a distribution similar to that of the refined sample as a whole (figure 5). Contrary to what would normally be expected, fainter objects can be identified spectroscopically if they have a strong Ly α emission line or a clear continuum break in a comparatively noise free region of the spectrum. These features can often make high redshift galaxies easier to identify than lower redshift objects without any emission lines. At low signal-to-noise, lower redshift objects can show essentially featureless continuum making any redshift determination difficult, if not impossible. As such, any observed objects which can not be identified in their spectra due to low signal-to-noise, often up to 50% of the observed sample, cannot be assumed to lie at high or low redshift; either scenario is possible.

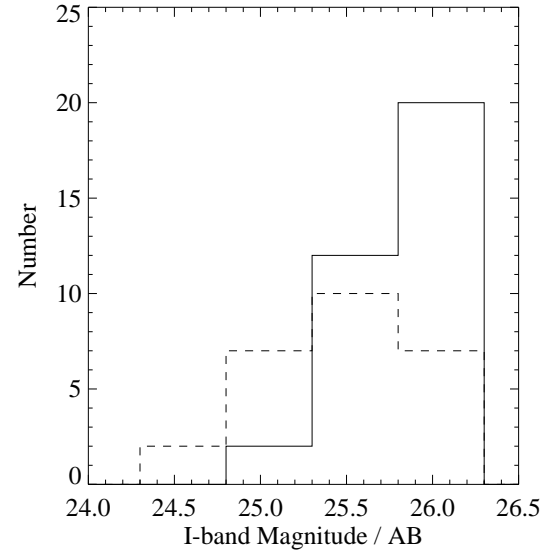


Figure 7. Distribution of I -band magnitudes for spectroscopically confirmed high redshift galaxies (solid line) and lower redshift objects (galaxies and stars, dashed line) within the raw photometric sample.

Of the 253 objects in the refined sample, 83 were observed on the spectroscopic masks. Within this subsample 33 objects were confirmed to lie at $z > 4.6$, 9 were identified as intermediate galaxies or stars and 41 were detected spectroscopically but the signal-to-noise was too low to allocate a firm identification. Of the identified objects, 20% were at a redshift lower than targeted. Using the K_s -band imaging, the fraction of high and low redshift objects in the unidentified sample is estimated.

While none of the individually confirmed high redshift galaxies were detected in K_s , by stacking 30 images we determined that their average colour was $I - K_s < 0.0$. Similarly, a typical colour for the confirmed low redshift sources and the unidentified objects was obtained. The nine confirmed low redshift sources gave colour of $I - K_s = 1.3$. 201 unidentified objects in the refined sample, including those observed spectroscopically but resulted in low signal-to-noise, had an average colour of $I - K_s = 0.3$. Where there was no detection in the stacked K_s -band image the 2σ limit for a $2''$ circular aperture was measured using background regions. Given the need for adequate background regions surrounding the central stack to estimate the depth of the image, a small number of sources were not included as they were positioned close to the edge of the near-IR field.

Assuming that the unidentified sample is a combination of the high ($I - K_s < 0.0$) and low redshift ($I - K_s = 1.3$) populations, the typical colours imply the unidentified sample contains at least $\sim 75\%$ high redshift objects and less than $\sim 25\%$ low redshift objects. Combining these results with the spectroscopic identifications gives a contamination fraction of $\sim 20\%$ for the refined sample. Applying the same technique to all optically selected objects including the near-IR detected objects, the contamination fraction is estimated to be around $\sim 40\%$. The unidentified near-IR

detected sources have an average colour of $I - K_s = 3.2$ (compared with a colour of $I - K_s = 2.6$ for the near-IR detected objects confirmed to be at low redshift) which implies a very high level of interloper within this subsample. The higher contamination rate estimated for the full sample clearly demonstrates the utility of the near-IR rejection of interlopers in addition to the purely optical selection.

There have been several other spectroscopic studies of $z \sim 5$ LBGs, for example Ando et al. (2007) and Vanzella et al. (2009). The differences in selection function and filter sets used in these studies makes a direct comparison of the level of contamination difficult. One feature that all high redshift spectroscopic surveys share is the large fraction of unidentified sources due to insufficient signal-to-noise in the spectroscopy. This can be up to 50% of the observed sample. Such studies can appear reliable because most or all of the spectroscopically identified objects are at high redshift, *e.g.* Ando et al. (2007) did not identify any lower redshift objects spectroscopically. However, care must be taken when assuming the same contamination rates for the spectroscopically unidentified sources and subsequently for the whole photometric sample, especially if only the brightest candidates have been targeted.

Although it is difficult to compare contamination fractions of different samples due to different selection, filters and instrument combinations (Stanway et al. 2008b), it seems that typical contamination rates are between 10% and 20%. Stanway et al. (2008b) shows that with contamination fractions of this level, measurements such as the angular correlation function of photometrically-selected LBG samples can be compromised because the expected contaminating population can themselves have a clear correlation signal. Also, the difference in optical-to-near-IR colour between contaminants and confirmed high redshift LBGs demonstrated here can also cause problems in estimating the typical multi-wavelength spectral energy distributions of LBGs. If a population of contaminants individually-undetected in the near-IR are combined in a stacking analysis with true LBGs, they will redden the resulting SED, and artificially inflate the estimated age of the stellar population in a typical LBG or dust fraction.

6 COMPLETENESS DETERMINATIONS

The completeness of the selection in each field was estimated by carrying out two kinds of simulations. The first is a simulation of recoverability which depends on the quality and depth of the imaging. This involved injecting artificial sources with known properties into our photometry data in order to determine the efficiency of SExtractor in recovering them. The second simulation investigated the effects of the selection criteria and image quality on a model spectrum.

6.1 Recoverability

For each field, 300,000 artificial galaxies were generated covering a range of magnitudes from 22.0 to 28.0 and a $R - I$ colour was assigned within the range 0.0 to 3.0. A surface brightness profile was chosen from a sample of four stellar profiles measured directly from the images to reflect the seeing conditions (the high redshift candidates are unresolved

in ground-based data), and a selection of HST/ACS images of two or more galaxies seen at small angular separations selected in the GOODS data of the Chandra Deep Field South (CDFS). The high resolution multiple systems were convolved with a Gaussian profile to match the ground-based seeing conditions and were chosen with the same frequency as seen in the CDFS ($\sim 20\%$) to mimic this population. Using the selected magnitude, colour and profile, a ‘simulated’ galaxy was created for the I -band and R -band images and placed at random coordinates within the field excluding previously masked areas near bright objects used in the photometric selection. By placing these galaxies directly onto the science image, the noise properties of the image were added to the simulated galaxy. The process was repeated one thousand times for each field as no more than 300 simulated galaxies were placed on any one image to prevent mutual overcrowding affecting the results.

Each new image with the simulated galaxies was processed through SExtractor in the same way as the original science data, creating catalogues containing the simulated galaxies as observed on the images. After these were matched with the original galaxy information on magnitude, colour and position, a catalogue was created containing the known simulated magnitudes and the recovered SExtractor magnitudes of each fake galaxy.

The high redshift galaxy candidates were selected on two main criteria, a magnitude limit and a colour cut. The recoverability of the galaxies using the high redshift selection of $I < 26.3$ and $R - I > 1.3$ was measured for a range of colours and magnitudes and is shown in the contour plots of figure 8. Eight of the ten fields show comparable results, with a completeness of 25% at the I -band flux limit. However two fields had consistently lower completeness which was caused by the two worst seeing conditions for the I -band observations, $0.73''$ compared to an average of $0.6''$ over the other eight fields. This spread the received flux over a larger area causing the objects to drop below the surface brightness limit. If the objects were detected, the photometry, made fainter by the seeing conditions, is corrected by the appropriate aperture corrections. Figure 8 shows an average of the ten survey fields, with the simulated I -band magnitude and $R - I$ colour along the x and y axes respectively. The contours are placed at 20%, 40%, 60%, 80% and 90% of inserted galaxies recovered, using the colour selection of $I < 26.3$ and $R - I > 1.3$. Figure 8 shows that the completeness of object recovery is generally independent of colour with the results reflecting the increasing photometric errors at fainter magnitudes. The maximum completeness never rises to more than $\sim 95\%$ due to object confusion despite areas near bright objects being masked.

Figure 8 implies that only 60% of galaxies with an intrinsic $R - I$ colour of 1.3 would be included in the sample. This is not surprising as only $\sim 50\%$ of objects would be expected to be included in the sample at the colour cut. Even a small photometric error in the R or I -band would cause the colour to become too blue. The applied $R - I$ colour criterion was chosen from the previous work of Lehnert & Bremer (2003) who found a colour cut of $R - I > 1.5$ selects galaxies at $z > 4.8$ using the same FORS2 filters used in this work and models from Fioc & Rocca-Volmerange (1997). By adopting a bluer colour cut, completeness at this selection colour is much higher. Although this could introduce a

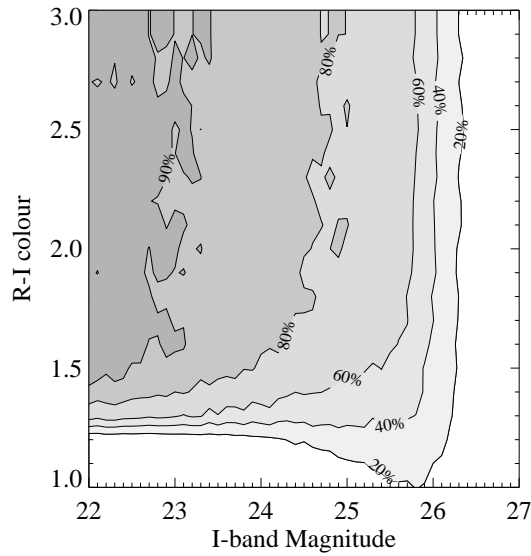


Figure 8. Contours illustrating the success rate of recovering galaxies within the high redshift colour selection. The levels shown are 20%, 40%, 60%, 80% and 90%. The x-axis is the original I -band magnitude of the ‘fake’ galaxy inserted into the images and the y-axis is the original colour assigned to this ‘fake’ galaxy. The contours show the percentage recovery rate of these ‘fake’ galaxies using the same method as the high redshift selection. It is shown that the completeness of object recovery is generally independent of colour with the results reflecting the increasing photometric errors at fainter magnitudes.

higher contamination fraction, the additional near-IR imaging should minimise this.

Also, the objects that were recovered with intrinsic colours bluer than our cut represent a population of objects that can contaminate the sample, rather than one that affects the sample completeness. These objects have their measured colours reddened by the statistical errors on the photometry. At $I = 26$ a substantial fraction ($\sim 20\%$) of objects with intrinsic $R - I = 1.1$ can be included in a sample with an observed cut of $R - I > 1.3$ given the photometric properties of our source data. Such objects are likely to be at $z < 4$ and could be a substantial contaminating population depending upon their luminosity function. In reality, such objects would often have significant V -band flux or near-IR detections which would rule them out of the high redshift candidate sample.

6.2 Effect of Selection Criteria

The second simulation determined the completeness of our final sample given the interplay of photometric cuts used to reject contaminants and the statistics of the photometry data, as a function of redshift. An artificial catalogue of 10^8 sources was generated with a I -band magnitude distribution determined by the $z = 5$ Bouwens et al. (2007) luminosity function. Each galaxy was assigned a redshift (in 0.01 redshift bins) which determined its I -band magnitude and $R - I$ colour assuming a flat spectrum in F_ν and accounting for IGM absorption using the modified Madau prescription as

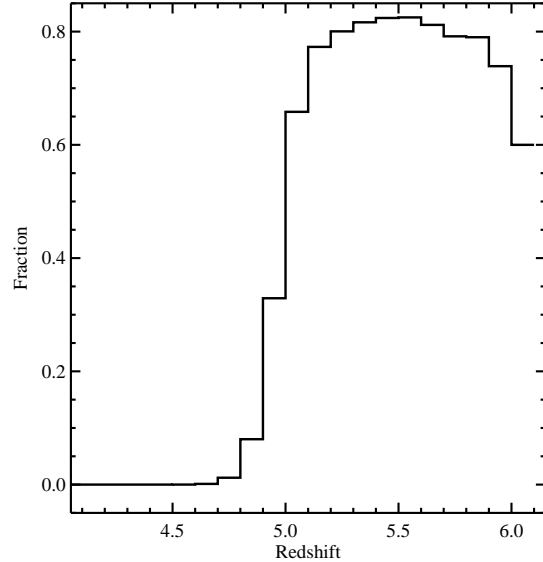


Figure 9. The fraction of galaxies recovered as a function of redshift with an intrinsic $I < 26.3$, $R - I > 1.3$ and $V > 27.5$ given the photometric errors of the imaging data. The luminosity function used to generate the predicted number counts was that measured in Bouwens et al. (2007) for $z \sim 5$.

a function of redshift (described in section 4.1). The V -, R - and I -band magnitudes of the artificial sources were then independently perturbed to match the typical noise properties of the imaging data and the typical weak lensing characteristics from the foreground clusters. The fraction of objects which were then recovered using the previous $z \sim 5$ selection criteria ($I < 26.3$, $R - I > 1.3$ and $V > 27.5$) as a function of redshift is shown in figure 9. In total, around 80% of galaxies at $5.0 < z < 6.0$ are selected using the photometric colour criteria of this work but completeness falls off rapidly below $z = 5$.

7 MORPHOLOGY

The morphologies of the high redshift candidates were studied using high resolution images from the Hubble Space Telescopes using the ACS camera and F814W filter which cover nine out of the ten survey fields. Each field was observed for 1 orbit with the central regions observed for a total of 5 orbits.

Catalogues from the HST/ACS images were created using SExtractor in order to obtain half-light radii for the potential high redshift galaxies. Only sources with the deepest, 5 orbit depth of data are discussed.

The majority of high redshift candidates in the refined sample were found to be resolved with individual peaky components. They have half-light radii between $0.1''$ and $0.26''$ (figure 10) which corresponds to a range of 0.3–1.6 kpc at a redshift of $z \sim 5$, with a mean value of $0.14''$ or 0.8 kpc in agreement with Bremer et al. (2004), the purely space-based sample of Conselice & Arnold (2009) and the higher redshift galaxies of Bouwens et al. (2006). A subset have formally unresolved radii ($\sim 0.06''$). However, these objects are

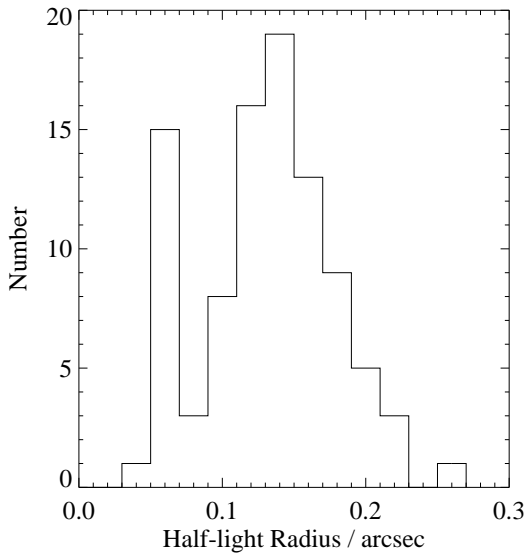


Figure 10. Distribution of half-light radii, in arcseconds, of the refined high redshift sample with the deepest HST data. Radii below $0.07''$ are unresolved.

generally faint with limited S/N that could be effecting the measurement and fitting procedures. While some of these could potentially be stars, their colours do not support this hypothesis. It is also possible to select AGN such as that described in Douglas et al. (2007) which could be unresolved in the HST imaging.

Over the 9 fields, 31 out of 95 (33%) candidates with deep HST data show disturbed or asymmetric morphology or are part of a multiple system on scales from $0.2''$ to $1.2''$ or 1.3kpc to 7.5kpc. Examples of multiple systems, which are not resolved in ground based imaging, are shown in figure 11. Each individual component has a half-light radius consistent with the isolated objects. It is not clear whether these are most likely to be multiple interacting systems or UV-bright knots in an underlying larger system.

Of the multiple systems, 10 candidates are close pairs and 4 are part of a larger collection of sources with a mean separation of $0.5''$. Objects with separation distances of more than $0.8''$ are barely resolved in the ground-based imaging and extend with the same orientation. The fractions of objects observed with multiple members (15%) agrees with the work of Conselice & Arnold (2009) in the Hubble Ultra Deep Field (HUDF) where $\sim 19\%$ of their V-drop sample were found to be in pairs. With this much deeper data, the possibility that the observed galaxy pairs are a larger object with UV bright peaks is less. As the sample fractions showing galaxies pairs for the deep HUDF sample and the sample presented here are similar, it is likely that these are the true pair fractions for each sample.

The 17 candidates which show disturbed or asymmetric morphology were identified visually. Even in the deepest available HST imaging the objects are small and faint making any detailed measurement of their structure challenging. For a similar sample in the HUDF, Conselice & Arnold (2009) observed the same fraction exhibiting asymmetric morphologies. With the much deeper observations of the

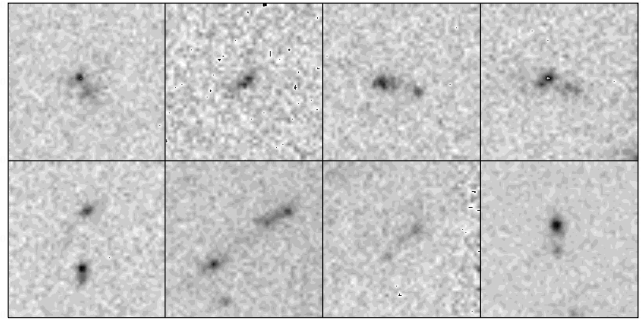


Figure 11. Examples of high redshift galaxy candidates with multiple components or disturbed morphology visible in the high resolution HST/ACS F814W imaging. Each image segment is $2.5'' \times 2.5''$.

HUDF, more precise measurements of the structure and potential asymmetry of the high redshift galaxy candidates was possible. Although only visual classification was used for the ERGS sample, the agreement of asymmetric sample fractions suggest that such a classification is reliable. It also suggests that the fraction of multiple of asymmetric systems does not change with UV luminosity over the range probed by the two studies.

8 THE UV LUMINOSITY FUNCTION

One apparently straightforward measurement of the properties of $z \sim 5$ LBGs that can be made with a photometric sample is the rest-frame observed UV luminosity function. For this to be reliable and meaningful, the contamination and completeness of the sample must be understood. While our reliable photometric sample is constrained to bright magnitudes in comparison to some published data (e.g. Bouwens et al. 2007), it can be used to explore the brighter end of the luminosity function.

In order to calculate a luminosity function which represents the observed luminosity distribution of galaxies, the following method, which is essentially the same as that used by Bouwens et al. (2007), was used. Monte carlo simulations were used to create artificial populations of LBGs across the redshift interval probed photometrically, with corrections for photometric errors, completeness and weak lensing. After an identical photometric selection, the resulting artificial LBG candidates represents what would be observed given the initial luminosity function assumed. When compared to the real, observed LBG candidates, a best-fitting intrinsic luminosity function can be found.

A range of Schechter luminosity functions (defined by the characteristic magnitude M^* , the faint end slope α and normalisation ϕ^*) were generated across a broad spectrum of parameters, from -19.65 to -21.45 in M_{UV}^* , faint end slopes, α , between -1.40 and -1.95 and ϕ^* fitted freely, and were compared to the observed number counts of the $z \sim 5$ galaxy candidates.

For each proposed luminosity function the following steps were used to create a catalogue of galaxies which reflects the assumed luminosity function and the properties of the observed fields. Within 0.01 redshift bins from $z = 4$ to $z = 6.1$, the luminosity distance, luminosity function and

IGM absorption were used to determine the apparent magnitude distribution and number density of objects scaled according to the volume within the redshift slice (per arcmin 2). The colours of the objects in this redshift bin were calculated according to the FORS2 instrumental response and filter profiles assuming the galaxies were flat in F_ν and incorporating Madau et al. (1999) IGM absorption with a higher density of absorbing systems at high redshift as discussed in section 4.1. The galaxy catalogues for each redshift bin were combined to create a sample with a magnitude, colour and redshift distribution which reflects the proposed luminosity function.

To simulate the properties of the survey fields, each galaxy in the artificial catalogue had colours and magnitudes perturbed by the photometric errors and typical weak lensing correction (*e.g.* if 20% of the survey area was lensed by 0.1 magnitudes, 20% of the catalogue was randomly selected and the model magnitudes were brightened.) Using this artificial catalogue, the galaxy candidates were reselected using the original selection criteria ($I < 26.3$, $R - I > 1.3$ and $V > 27.5$) to produce the predicted magnitude distribution for the ERGS survey for the assumed luminosity function with magnitude dependent completeness corrections (as described in section 6) in addition to the photometric errors, caused by the ERGS image quality, and weak lensing corrections.

Having repeated this procedure for each combination of luminosity function parameters, the predicted and observed number counts were compared using χ^2 statistics across the range of M^* and α , allowing the normalisation, ϕ^* to vary. The resulting best fitting observed luminosity function is shown in figure 12. As this method does not formally fit ϕ^* , the correction for contamination is applied to the normalisation after the fitting procedure.

As figures 12 and 13 show, our results for the refined sample, are generally in agreement with those of Bouwens et al. (2007). That result was derived from extremely deep multi-band HST imaging of a comparatively small area. The fidelity of the data means that it produces an intrinsically cleaner sample with less contamination than typical ground-based studies. We determined a formal best-fitting $M^* = -20.96 \pm 0.2$ at 1500Å, 0.3 magnitudes fainter than that found by Bouwens et al. (2007) (see also Oesch et al. 2007; Beckwith et al. 2006; Yoshida et al. 2006, for additional space and ground-based studies) with $\alpha = -1.4$. Given that the best-fitting M^* falls into one of the faintest bins used for model fitting, the data set in this paper can not constrain the faint end slope (figure 13). When α was set to -1.6 the χ^2 best fitting characteristic magnitude was $M^* = -20.9 \pm 0.2$ and $\phi^* = 1.1 \pm 0.2 \times 10^{-3}$ Mpc $^{-3}$ agreeing, within the errors, with previous studies. As we are observing $z = 5$ LBGs using an I -band filter at 7680Å the measured luminosity function is at 1250Å compared to 1600Å luminosity function in Bouwens et al. (2007). Such a difference in wavelength would result in different luminosity function parameters at lower redshift, due to the spectral slope of the source. As high redshift LBGs have relatively flat continuum, particularly between 1250Å and 1600Å changes in the luminosity function parameters are expected to be small.

Assuming the luminosity function fitted to the refined sample defines the shape of the relationship, the normalisation, as defined by ϕ^* , can be adjusted to include the relia-

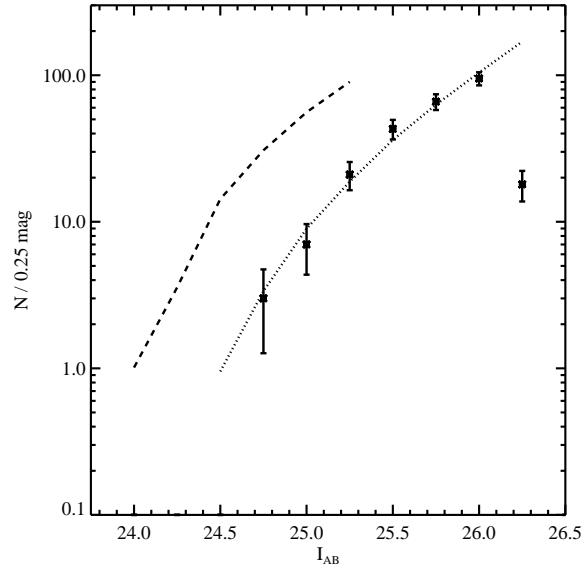


Figure 12. The observed galaxy number counts across the 10 survey fields compared to the best fitting Schechter luminosity function (dotted line) with $\alpha = -1.6$ fixed. Steidel et al. (1999) $z \sim 4$ luminosity function applied to $z = 5$ assuming no evolution and given the imaging properties and selection of this study is shown by the dashed line. The faintest I -band magnitude bin was not included in the fitting procedure. The errors shown are the Poissonian errors of the number of objects in each bin.

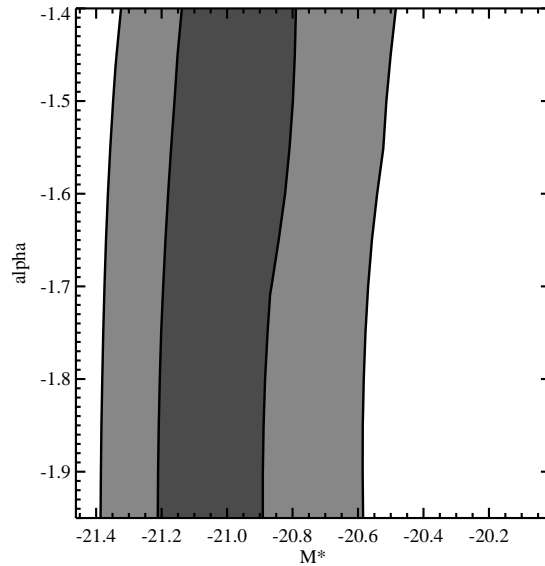


Figure 13. χ^2 space illustrating the fitting of Schechter functions to the observed galaxy number counts. The contours levels are 90%, 95% probabilities. With such a faint M^* relative to the depth of the sample, the slope of the faint-end, α , can not be constrained with this data.

bility of this sample ($\sim 80\%$, see section 5.2). The adjusted normalisation gives $\phi^* = 0.9 \pm 0.2 \times 10^{-3} \text{ Mpc}^{-3}$ where the fraction of objects at high redshift is assumed to be constant with apparent magnitude. However, figure 5 suggests that contamination is a more significant problem at brighter magnitudes with a high fraction of lower redshift objects compared to high redshift candidates. A magnitude dependant contamination correction, with a larger correction in the brightest bins, would change the shape of the luminosity function leading to a fainter M^* . Even with the extensive spectroscopic followup carried out in the ERGS project, the number of confirmed high redshift galaxies is not sufficient to study the reliability of the photometric sample as a function of apparent magnitude.

For consistency with other work, we have used a Schechter (1976) luminosity function form for fitting. We note that the suitability of an analytic form derived from the expected form of galaxy mass functions is questionable for these intense starburst events. The UV emission arising from these LBGs is highly stochastic, tracing as it does short lived intense star formation events. The characteristic timescale for these is $\sim 30 \text{ Myr}$ (Verma et al. 2007) in comparison to a survey window of 250 Myr, *i.e.* the measured UV luminosity function is only capturing a fraction of the overall LBG population. The UV luminosity function is therefore likely to be weakly related to mass distribution of star forming galaxies at these redshifts and therefore there is little *a priori* reason to expect it to follow a Schechter function. Indeed, it is plausible that the UV luminosity function is shaped by the time-dependent decay of UV emission from these short-lived starbursts, in effect the shape of the luminosity function mirrors the UV emission (and therefore star formation) history of a typical $z \sim 5$ LBG starburst. Although our data can be fit by a Schechter function, it can be equally well fit by a simple power-law, $N(L) \propto L^{-2.1}$. The main issue associated with determining the detailed UV luminosity function from bright to faint magnitudes at this redshift is the limited volume probed to the faintest levels. This necessitates combining together the number counts from at least two separate samples covering the bright and faint ends of the function. As these come from different volumes, the normalisation of the two ends can vary due to field-to-field variation caused by cosmic variance, or by magnitude-dependent contamination levels within the samples. Indeed, an intrinsic power law extending from bright to faint levels could manifest an apparent break if the bright and faint regimes were determined from separate samples and the bright subsample was normalised high due to cosmic variance or a higher level of magnitude-dependent contamination.

8.1 Sources of Reionization

Lehnert & Bremer (2003) claimed that the number of $z > 5$ sources, selected in a similar manner to this work, was less than that expected from the $z = 4$ luminosity function of Lyman Break galaxies (about 1/3 the number of sources for $I < 26.3$), assuming no evolution between the epochs. Although their data was taken with the same instrument as used in this work, their conclusion was drawn from only 10% of the sky area of this survey. Nevertheless, our average number counts over 10 fields also implies a similar lack of bright sources compared to that expected if there was no

evolution in the luminosity function between $z = 5$ and $z = 4$.

Figure 12 compares the observed galaxy number counts (crosses) with that predicted using Steidel et al. (1999) $z = 4$ luminosity function down to M^* . It can be seen that the observed number counts are a factor of ~ 3 less than would be expected if there is no evolution in the luminosity function between $z \sim 5$ and $z \sim 4$, a deficit which increases with luminosity. Although the epoch of reionization has ended by $z \sim 5$, the Universe still requires a sufficient density of UV photons to counteract the process of recombination and keep the hydrogen ionised. Even without the removal of contaminants, there is a lack of galaxies providing ionising photons at these magnitudes.

The equation for the density of star-formation required for reionization from Madau et al. (1999), modified to the cosmology assumed in this study, was used to estimate the star-formation density required to maintain the ionisation state of hydrogen at a redshift of 5.1, the mean redshift of the spectroscopically confirmed galaxies within the photometric sample. The concentration factor of hydrogen was assumed to be 30 and the photon escape fraction used was $f_{esc} = 0.14$ (Shapley et al. 2006), however these values are not well constrained and can vary largely. The total luminosity of the sample was found by converting all apparent magnitudes assuming the mean redshift of the confirmed high redshift galaxies within the sample for all objects. This was then converted to a star-formation rate using the relation given in Madau et al. (1998).

It was found that the star-formation density of the refined sample is a factor of ~ 4 lower than that necessary to maintain the ionisation of hydrogen at redshift ~ 5 . Even when the whole photometric sample is used, without the removal of likely contaminants, the star-formation density is still nearly 3 times lower than required. These results imply that the majority of ionising photons originated from fainter sources below the observed flux limit, ($I > 26.3$; Lehnert & Bremer 2003) even after the Universe has fully reionized. Another potential source of ionising photons are AGN. However, Bremer et al. (2004) and Douglas et al. (2007) have shown that the density of AGN at these redshifts is very low and as such can not be a large contributor to the overall photon budget of the Universe at these redshifts.

9 CONCLUSIONS

Through a photometric colour selection we have produced a sample of 253 high redshift Lyman Break Galaxy candidates at $z \sim 5$ drawn from 10 widely-separated fields with V, R, I, z, J, K_s photometry covering 275 arcmin 2 . Using simulations and a comparatively large programme of follow-up spectroscopy we have been able to determine the completeness and reliability of the sample. The sample of 253 sources is approximately 80 per cent reliable (*i.e.* has a ~ 20 per cent contamination rate). Even with multiple photometric bands used to select objects, the relatively extreme colours of dropout galaxies make them vulnerable to systematic effects in photometry of individual objects. Consequently, statistical results derived from large samples of photometrically-selected objects may well be prone to bias

or error because of contamination within the samples. As has been pointed out elsewhere (e.g. Stanway et al. 2008b), contamination rates of only 15 per cent can significantly skew some statistical results.

A large fraction of these galaxies have multiple components on scales probed by HST imaging. It is currently unclear whether the components are separate galaxies, or UV luminous regions embedded in a larger, darker underlying galaxy but deeper HUDF studies suggest we are observing multiple galaxy systems. Previous work has shown that LBGs appear to decrease in linear size with increasing redshift (Bouwens et al. 2004). This applies to individual components of multiple systems, but clearly not necessarily the systems themselves.

Contamination is a potentially serious issue in constraining the $z \sim 5$ luminosity function. Having taken into account our detailed reliability analysis, we confirm a decline of a factor of ~ 3 in the bright end of the luminosity function (to M^*) from $z = 4$ to $z = 5$. Assuming a Schechter fit to the UV luminosity function at $z \sim 5$, we obtain values for $M_{UV}^* = -20.9 \pm 0.2$ and $\phi^* = 0.9 \pm 0.2 \times 10^{-3} \text{ Mpc}^{-3}$ (with a magnitude independent correction for completeness), in agreement with Bouwens et al. (2007) and others. However, we question the basis for the use of a Schechter function. This is a proxy for a mass function, whereas the UV luminosity of LBGs arises from highly stochastic, short-lived starburst phases and should not necessarily correlate with the mass of the underlying system.

ACKNOWLEDGEMENTS

We thank the referee for their helpful comments. LSD acknowledges support from P2I. ERS acknowledges support from STFC. Based on observations made with ESO Telescopes at the La Silla and Paranal Observatory under programme IDs 166.A-0162 and 175.A-0706. Also based on observations made with the NASA/ESA Hubble Space Telescope, obtained at the Space Telescope Science Institute, which is operated by the Association of Universities for Research in Astronomy, Inc., under NASA contract NAS 5-26555. These observations are associated with program 9476. We thank the members of the EDics collaboration for creating an imaging dataset with a usefulness far beyond their original intent.

REFERENCES

- Ando M., Ohta K., Iwata I., Akiyama M., Aoki K., Tamura N., 2007, PASJ, 59, 717
- Appenzeller, I., et al. 1998, The Messenger, 94, 1
- Beckwith S. V. W., et al., 2006, AJ, 132, 1729
- Bertin, E., & Arnouts, S. 1996, A&AS, 117, 393
- Bouwens, R. J., Illingworth, G. D., Blakeslee, J. P., Broadhurst, T. J., & Franx, M. 2004, ApJ, 611, L1
- Bouwens R. J., Illingworth G. D., Blakeslee J. P., Franx M., 2006, ApJ, 653, 53
- Bouwens, R. J., Illingworth, G. D., Franx, M., & Ford, H. 2007, ApJ, 670, 928
- Bremer, M. N., Lehnert, M. D., Waddington, I., Hardcastle, M. J., Boyce, P. J., & Phillipps, S. 2004, MNRAS, 347, L7
- Bunker, A. J., Stanway, E. R., Ellis, R. S., & McMahon, R. G. 2004, MNRAS, 355, 374
- Calzetti, D., Armus, L., Bohlin, R. C., Kinney, A. L., Koornneef, J., & Storchi-Bergmann, T. 2000, ApJ, 533, 682
- Clowe, D., et al. 2006, A&A, 451, 395
- Conselice C. J., Arnold J., 2009, MNRAS, 397, 208
- Desai, V., et al. 2007, ApJ, 660, 1151
- Douglas, L. S., et al. 2009, MNRAS submitted
- Douglas, L. S., Bremer, M. N., Stanway, E. R., & Lehnert, M. D. 2007, MNRAS, 376, 1393
- Fioc M., Rocca-Volmerange B., 1997, A&A, 326, 950
- Gonzalez, A. H., Zaritsky, D., Dalcanton, J. J., & Nelson, A. 2001, ApJS, 137, 117
- Guhathakurta, P., Tyson, J. A., & Majewski, S. R. 1990, ApJ, 357, L9
- Hawley, S. L., et al. 2002, AJ, 123, 3409
- Knapp, G. R., et al. 2004, AJ, 127, 3553
- Lehnert, M. D., & Bremer, M. 2003, ApJ, 593, 630
- Madau P., Pozzetti L., Dickinson M., 1998, ApJ, 498, 106
- Madau, P., Haardt, F., & Rees, M. J. 1999, ApJ, 514, 648
- Maraston, C. 2005, MNRAS, 362, 799
- Oesch P. A., et al., 2007, ApJ, 671, 1212
- Oke, J. B., & Gunn, J. E. 1983, ApJ, 266, 713
- Ouchi, M., et al. 2004, ApJ, 611, 660
- Schlegel, D. J., Finkbeiner, D. P., & Davis, M. 1998, ApJ, 500, 525
- Schechter, P. 1976, ApJ, 203, 297
- Shapley A. E., Steidel C. C., Pettini M., Adelberger K. L., Erb D. K., 2006, ApJ, 651, 688
- Songaila A., 2004, AJ, 127, 2598
- Stanway, E. R., Bunker, A. J., & McMahon, R. G. 2003, MNRAS, 342, 439
- Stanway, E. R., Bunker, A. J., McMahon, R. G., Ellis, R. S., Treu, T., & McCarthy, P. J. 2004, ApJ, 607, 704
- Stanway, E. R., Bremer, M. N., Squitieri, V., Douglas, L. S., & Lehnert, M. D. 2008a, MNRAS, 386, 370
- Stanway, E. R., Bremer, M. N., & Lehnert, M. D. 2008b, MNRAS, 385, 493
- Steidel, C. C., & Hamilton, D. 1992, AJ, 104, 941
- Steidel, C. C., & Hamilton, D. 1993, AJ, 105, 2017
- Steidel, C. C., Adelberger, K. L., Giavalisco, M., Dickinson, M., & Pettini, M. 1999, ApJ, 519, 1
- Steidel C. C., Adelberger K. L., Shapley A. E., Pettini M., Dickinson M., Giavalisco M., 2003, ApJ, 592, 728
- Trenti M., Stiavelli M., 2008, ApJ, 676, 767
- Vanzella E., et al., 2009, ApJ, 695, 1163
- Verma, A., Lehnert, M. D., Förster Schreiber, N. M., Bremer, M. N., & Douglas, L. 2007, MNRAS, 377, 1024
- White, S. D. M., et al. 2005, A&A, 444, 365
- Yoshida M., et al., 2006, ApJ, 653, 988